© Copyright 2021

Lillian Thiel

Post-Fabrication Trimming of Gallium Phosphide Ring Resonators for Quantum Frequency Conversion

Lillian Thiel

A thesis

submitted in partial fulfillment of the

requirements for the degree of

Master of Science in Electrical Engineering

University of Washington

2021

Committee:

Kai-Mei Fu, Chair

Arka Majumdar

Program Authorized to Offer Degree:

Electrical and Computer Engineering

University of Washington

Abstract

Post-fabrication trimming of gallium phosphide ring resonators for
quantum frequency conversion

Lillian Thiel

Chair of the Supervisory Committee:
Associate Professor Kai-Mei Fu
Physics and Electrical Engineering

Post-fabrication resonator trimming will be a critical tool in realizing long distance transmission of quantum states via frequency conversion with photonic ring resonators. Two trimming mechanisms are investigated: digital etching via separated diffusion-limited formation and removal of an oxide layer to modify resonator dimensions, and hydrogen silsesquioxane (HSQ) electron-beam exposure to modify cladding refractive index. Controlled etch cycles with resonant wavelength shifts of -0.379 ± 0.163 nm are demonstrated with digital etching. HSQ cladding electron-beam exposure shows a clear relationship between dose and wavelength shift that enables deterministic trimming of individual devices with quality factors on the order of 10^4 to within 0.03 nm of a target wavelength. HSQ electron-beam exposure is used to demonstrate target-wavelength-trimmed second harmonic generation from telecom to near infra-red wavelengths.

TABLE OF CONTENTS

Chapter 1. Introduction 1

1.1 Second Harmonic and Difference Frequency Generation in Ring Resonators 2

1.2 Resonant Wavelength Modification 4

Chapter 2. Background 7

2.1 Ring Resonator Theory 7

2.1.1 Basic Principles 7

2.1.2 Effective Index of Refraction 8

2.2 Second Harmonic Generation 9

2.3 Resonance Modification Simulations 10

Chapter 3. Background 14

3.1 Ring Resonator Design and Fabrication 14

3.1.1 Digital Etching Experiment Devices 14

3.1.2 HSQ Exposure Experiment Devices 15

3.2 Testing Setups 17

Chapter 4. Digital Etching 19

4.1 Background 19

4.2 Simulations 19

4.3 Experiment 20

4.4 Results 21

4.5 Conclusion 24

Chapter 5. HSQ exposure 26

5.1 Background 26

5.2 Simulations 27

5.3 Experiment 27

5.4 Results 28

5.5 Conclusion 32

Chapter 6. SHG with Target-Wavelength Trimming 34

6.1 Experiment 34

6.2 Second Harmonic Generation in Trimmed Resonators 36

6.3 Conclusion 37

Chapter 7. Conclusion and Outlook 39

LIST OF FIGURES

Figure 1.1. Wavelength dependence of light attenuation in optical fiber [3] 2

Figure 2.1. Ring diagram and sample transmission spectrum 7

Figure 2.2. Plot of solution space for single-mechanism shifting................................... 12

Figure 2.3. Plot of solution space for two-mechanism shifting. 13

Figure 3.1. Digital etching device layout 14

Figure 3.2. HSQ exposure device layout 16

Figure 4.1. Plot of cumulative wavelength shift during digital etching process.............. 22

Figure 4.2. Plot of resonance shift of single device during native oxide formation. 23

Figure 4.3.: Tilted SEM image of resonator sidewalls. Ring sidewall roughness clear in boxed region. 24

Figure 5.1. Diagram of (a) cage-form structure and (b) network-form structure of HSQ. 26

Figure 5.2. Plot of fundamental wavelength shifts for first dosage test. 29

Figure 5.3. Plot of second harmonic wavelength shifts for first dosage test. 29

Figure 5.4. Plot of fundamental wavelength shifts for second dosage test. 30

Figure 5.5. Plot of five-day resonance drift for fundamental wavelength 31

Figure 5.6. Distribution of normalized change in total quality factor at fundamental frequency 32

Figure 6.1. Predicted trimming behavior of identical SHG resonators............................ 34

Figure 6.4. Target-wavelength SHG for three identical devices 36

Figure 6.5. Temperature-tuning plots for devices 1, 2, 3.. 36

Figure 6.6. NIR transmission of Device 1 and Device 2 37

LIST OF TABLES

Table 2.1. Simulation Results for Fundamental Wavelength 11

Table 2.2. Simulation Results for Second Harmonic Wavelength 11

ACKNOWLEDGEMENTS

Thank you to Kai-Mei for giving me such an incredible learning opportunity as an undergraduate and supporting me as I transitioned towards graduate studies. Thank you to Alan and Sri for your guidance on this project, and to the whole lab for helping me discover my passion for research.

CHAPTER 1. INTRODUCTION

The development of chip-based photonic quantum circuits will enable large-scale implementation of emerging technologies including quantum communication by utilizing well-established nanofabrication techniques. In addition to single-photon sources, single-photon detectors, and photonic components for routing and interaction of light on-chip, robust photonic quantum circuits will need frequency conversion elements for interfacing quantum circuits with different qubits or with other photonic platforms such as fiber networks [1]. For example, multi-node entanglement of solid-state qubits via fiber optical links spanning up to 1.3 kilometers has been demonstrated with nitrogen-vacancy centers in diamond (photon emission at 637 nm), with the link length primarily limited by photon loss through the fiber interconnects [2, 3, 4]. Photonic quantum circuits need to efficiently convert light from single photon sources in the visible/NIR range (600 to 900 nm) to the telecom range (1400 to 1600 nm) to enable the transmission of quantum states over long distances. Photons emitted from several different solid-state qubit candidates attenuate at more than ten times the rate of photons with wavelengths in the telecom C-band when transmitted through optical fibers (Fig 1.1). To advance beyond proof-of-concept, lab-scale demonstrations of distributed entanglement will require the reliable transmission of individual photons across long distances. For visible/NIR emitting solid-state defects, attenuation may be minimized with nanophotonic devices which convert light from the visible/NIR to the IR range using quantum frequency conversion.

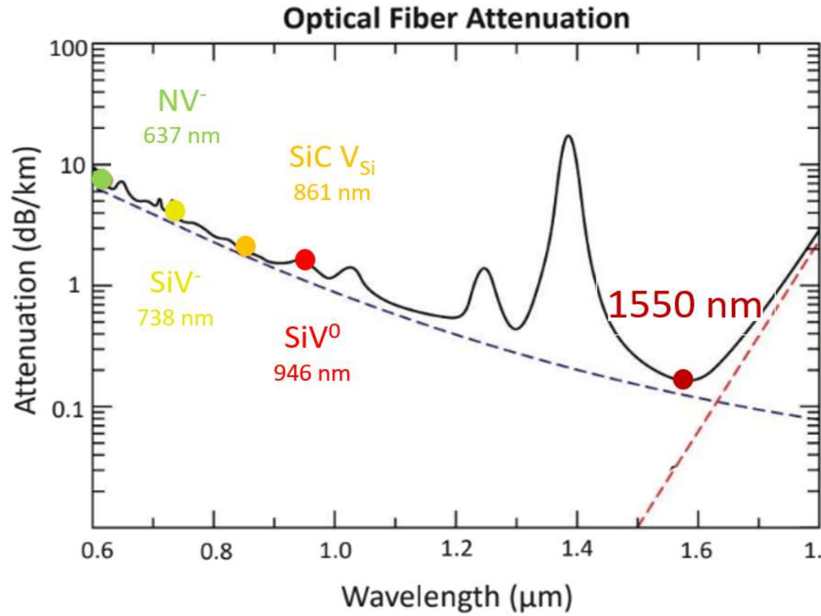

Figure 1.1. Wavelength dependence of light attenuation in optical fiber [5]

1.1 Second Harmonic and Difference Frequency Generation in Ring Resonators

Quantum frequency conversion is typically accomplished by exciting bulk materials that exhibit a non-linear optical susceptibility. The efficiency of the photon conversion process is dependent on the electric field intensity within the material. Nanophotonic devices like ring resonators can achieve efficiencies orders of magnitude higher than bulk materials by enhancing the electric field at specific resonant wavelengths inside the resonator. This enhancement is determined by the quality factor of the resonator at each wavelength involved in the frequency conversion process. Typically, ring resonators have quality factors on the order of 10^4 or higher at 1550 nm, which correspond to resonances with linewidths of tens of picometers [6]. Resonator designs for materials with a $\chi^{(2)}$ linearity may support either frequency doubling (via second harmonic generation in, in which light is converted from a single input to its second harmonic), or the

three-wave mixing process (difference frequency generation, in which light from two input frequencies produces light with a frequency equal to the difference between the two inputs). Resonators for use in quantum photonic circuits will eventually need to use difference frequency generation to convert visible/NIR light from solid-state defects to telecom wavelengths, however with only two rather than three resonances, devices for second harmonic generation present a more approachable initial problem to consider. For a ring to efficiently convert light from one frequency to another by SHG (DFG), its two (three) resonances must be tuned to satisfy the relative wavelength criteria for frequency conversion.

Ring resonators made of gallium phosphide (GaP) provide a strong candidate for efficient frequency conversion. GaP has a $\chi^{(2)}$ second-order non-linearity of $\sim$100 pm/V [7]. In addition to its large second-order non-linearity, GaP possesses several other qualities that make it a promising material for quantum information applications. High-quality thin films (~200 nm) of single crystal GaP can be epitaxially grown on silicon and Al_xGa_yP, allowing easy transfer to various substrates enabling hybrid photonic architectures. The high index of refraction (n = 3.3) compared to traditional non-linear materials ($LiNbO_3$, n = 2.3) enables the design of ultra-low mode volume resonators on a high-index diamond (n = 2.4) substrate, with the diamond hosting multiple promising near-surface solid-state qubit candidates including nitrogen-vacancy centers and silicon-vacancy centers [8, 9]. Given the wide bandgap of GaP (bandgap of 2.25 eV at 300 K), visible/NIR photons emitted by the qubits can be evanescently coupled to resonator modes [10]. Second harmonic generation from 1550 nm to 775 nm has been demonstrated with gallium phosphide on oxide ring resonators with an efficiency up to 400%W^{-1} [6].

1.2 Resonant Wavelength Modification

Due to nanoscale differences in fabrication, the resonances of the fabricated rings rarely match their designed values. Few devices possess the aligned resonances at both (SHG) or all three (DFG) process wavelengths necessary for maximally efficient frequency conversion. This challenge motivates the need for methods by which the resonant wavelength of a device may be modified post-fabrication. Altering the physical properties of a ring including ring width, height, resonator material refractive index, and cladding material refractive index enables the necessary control over resonant wavelength. Resonances may be either tuned via processes that require constant active control or trimmed via processes that permanently change device parameters. Resonant wavelength modification of ring resonators for frequency conversion processes presents a particularly complex challenge due to the simultaneous involvement of multiple wavelengths. Any tuning or trimming process will cause a shift in both absolute resonant wavelength and relative spacing between the two or three required resonances.

A few tuning and trimming techniques have already been established for ring resonators used in applications both including and beyond quantum frequency conversion. Temperature tuning leverages the thermo-optic effect, heating the ring to change the resonator material's index of refraction. Wet etching may reduce resonator width and height. Both have been used in SHG demonstrations, however these experiments have relied on fabricating hundreds of devices in order to find a select few (<8% device yield [6, 11]) with the right set of resonant wavelengths. In order to advance chip-based photonic circuits towards becoming a realistic and scalable technology, we must have consistent and high-level control over device resonances. Achieving this goal will require the identification and development of multiple independent tuning and trimming techniques.

In mapping out our requirements for identifying robust tuning and trimming techniques, we must consider the specific demands of scalable photonic frequency conversion devices. Frequency conversion efficiency depends on both the quality factor of the ring and the overlap of the fundamental and second harmonic modes. Any technique should maintain the quality factor of the device, which may be degraded by increased scattering losses as a result of elevated material surface roughness. For frequency conversion, the tuning mechanism should remain lossless over a wide range of wavelengths. Tuning or trimming devices varying from their designed resonances due to fabrication tolerances will require high resolution over small ranges of wavelengths. Thus, resolution of a tuning or trimming mechanism supersedes range. The guiding principle of technology scalability contributes additional requirements. Any permanent tuning technique must also be easily reproducible on other devices. The modifications to the device should remain stable over time, ideally under atmospheric and room temperature conditions. Finally, a complete set of tuning techniques should include methods that can target single devices in addition to bulk processing methods.

In this work, I discuss two post-fabrication trimming techniques: digital etching as a width modification mechanism, and exposure of hydrogen silsesquioxane (HSQ) electron-beam resist as a cladding refractive index modification mechanism. Through both simulations and physical experimentation, I assess the degree to which these mechanisms fulfill the criteria I have defined above. Digital etching successfully blue-shifts devices through sub-nanometer steps over the range required for identical device trimming. However, the stability and accuracy of digital etching are complicated by formation of a native oxide layer. HSQ exposure proves to be an exceptionally useful process with high resolution, an appropriate trimming range, and easy adjustment of single devices. Using the results of my work on HSQ exposure trimming, I

demonstrate successful target-wavelength second harmonic generation with multiple devices on the same chip.

CHAPTER 2. BACKGROUND

2.1 Ring Resonator Theory

2.1.1 *Basic Principles*

Ring resonators work via constructive interference: light from a waveguide evanescently couples into the cavity, and as it travels around the ring (Fig. 2.1.a), it interferes with new light coupling into the cavity and itself. If the fields are in phase with each-other, they interfere constructively. The light must satisfy the condition:

$$2\pi r = m\frac{\lambda_0}{n_{eff}} \tag{2.1}$$

where azimuthal mode number m is the integer number of wavelengths around the ring. r is the radius of the ring and n_{eff} is the effective index of refraction of the ring which depends on the waveguide curvature, material, ring width, ring height, and cladding, as well as the radial mode of the light. When this condition is satisfied, the incident electric field is greatly enhanced within the cavity. Resonant wavelengths correspond to Lorentzian dips (Fig. 2.1.b) in intensity of transmitted signal at the through port (Fig 2.1.a) from the electric field built up in the cavity.

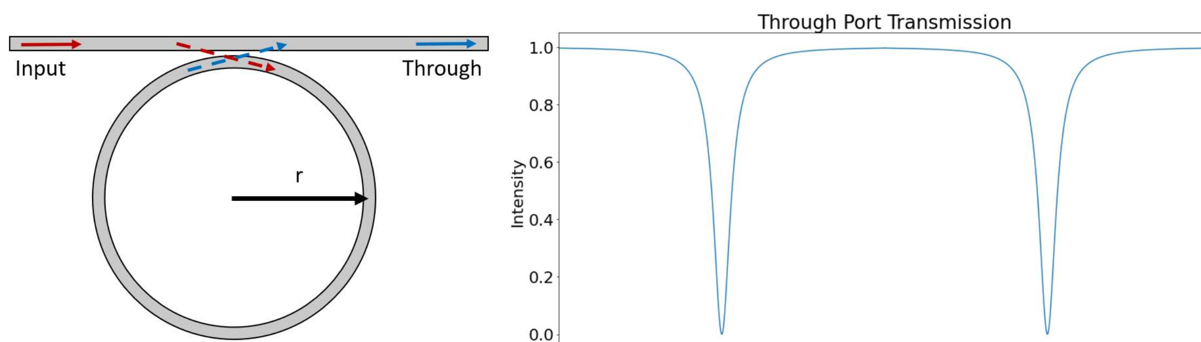

Figure 2.1. Ring diagram and sample transmission spectrum.

The quality factor of a resonator acts as a measure of the lifetime of a photon inside the cavity, and thus reflects the degree of enhancement of electric field at a resonant wavelength. The total quality factor Q_T is defined as the ratio of the resonant frequency υ to the photon loss rate κ_T, and relates to the intrinsic quality factor Q_i and the coupling quality factor, Q_c.

$$Q_T = \frac{\upsilon}{\kappa_T} = \frac{\upsilon}{\Delta\nu} = \frac{Q_i Q_c}{Q_i + Q_c} \tag{2.2}$$

The intrinsic quality factor represents radiative, scattering, and absorption losses as light travels around the ring. The coupling quality factor represents loss from light coupling into the waveguide from the cavity.

2.1.2 *Effective Index of Refraction*

The effective index of refraction, n_{eff}, determines the propagation of a specific mode in the resonator. It is defined as the ration of the propagation constant of the mode, β_m to the free space wavenumber, k_0.

$$n_{eff} = \frac{\beta_m}{k_0} \tag{2.3}$$

The propagation constant β_m for a mode reflects the fact that not all the light from the mode is traveling in the same medium: some travels outside the waveguide material. It may be found by solving Maxwell's equations for the specific mode and waveguide geometry. Thus, the effective index of refraction will depend upon the waveguide curvature, waveguide dimensions, waveguide material, cladding material, and radial light mode.

2.2 SECOND HARMONIC GENERATION

At low input powers, the SHG conversion efficiency of power P between modes 1 and 2 with angular frequencies $\omega_1$and ω_2 is given by:

$$\frac{P_{2,out}}{P_{1,in}^2} = \frac{|\chi^{(2)}|^2}{\epsilon_0 \lambda_1^3} |\bar{\beta}|^2 \frac{2}{\omega_1} \frac{Q_1^4 Q_2^2}{Q_{c1}^2 Q_{c2}} \tag{2.4}$$

where $\chi^{(2)}$ is the non-linear susceptibility of the material, Q_1 and Q_2 the total resonator quality factors at ω_1 and ω_2 ($1/Q_1 = 1/Q_{i1} + 1/Q_{c1}$), and $\bar{\beta}$ the nonlinear overlap of the electric fields for the fundamental and second harmonic modes [12]. The nonlinear coupling figure of merit $\bar{\beta}$ encompasses information about the mode volume of interaction and the phase-matching for the cavity.

$$\bar{\beta} = \frac{\int \sum_{i \neq j \neq k} \left(E_{1i} E_{2j}^* E_{1k} + E_{1i} E_{2k}^* E_{1j} \right) dr}{\left(\int \epsilon_1 |E_1|^2 \, dr \right) \sqrt{\int \epsilon_2 |E_2|^2 \, dr}} \tag{2.5}$$

For common resonators like rings and photonic crystals, the contribution of $\bar{\beta}$ to the conversion efficiency is constrained by resonator geometry and material nonlinearity. Thus, the quality factor of the resonator at the process wavelengths is critical to ensuring the necessary efficiency for single-photon conversion.

Any newly converted light must be in phase with previously converted light, else destructive interference between fields may occur. Ideally the phase mismatch Δk between modes should be zero, however material dispersion makes meeting this condition impossible in materials like GaP. Instead, periodic changes in the sign of $\chi^{(2)}$ may be used to compensate and avoid back-conversion via quasi-phase-matching. For ring resonators made of (100)-normal zincblende

crystals like GaP, the sign of the $\chi^{(2)}$ tensor changes sign every 90°, allowing for quasi-phase-matching [13]. Additionally, based on the form of $\chi^{(2)}$ in this class of materials, only mutually perpendicular field components contribute to frequency conversion, leading to the choice of one TM and one TE mode for the process. Based on these physical constraints, the quasi-phase-matching condition that the ring must meet to maximize the mode overlap integral $\bar{\beta}$ is $2m_1 = m_2 \pm 2$, where m_1 and m_2 are the fundamental and second harmonic azimuthal mode numbers respectively.

2.3 Resonance Modification Simulations

Every change in the physical parameters of a ring resonator will cause some change in effective index of refraction and therefore change in resonant wavelength. For a ring with multiple resonances at very different wavelengths, the rate of change of resonance with respect to any parameter is different. For a ring with resonances near 775 nm and 1550 nm, both the absolute wavelength of each resonance and the relative spacing between resonances will shift. By looking at simulations of the relationship between resonant wavelength and the physical parameters that we have control over, we can visualize how multiple post-fabrication tuning and trimming mechanisms are critical in enabling the integration of frequency conversion elements into quantum networks. I will discuss how the ring width and refractive indices of ring material and cladding affect resonant wavelength.

Take as an example a doubly resonant GaP device with three different tuning mechanisms with resonance shift rates at 775 nm and 1550 nm as shown in Table 2.1 and 2.2. These rates and their respective parameter spaces reflect real physical processes that will be discussed later in this

work. The device simulated is a design from Ref. [6] used to demonstrate efficient SHG from 1550 nm to 775 nm. The design consists of a 427 nm-thick GaP membrane on SiO_2, with a waveguide width of 840 nm and radius 7.14 µm (measured from the center of the waveguide). The top surface of the GaP is covered with a ~100 nm thick layer of HSQ resist left over from the fabrication process. The dependence of n_{eff} on temperature (affecting ring refractive index), ring width, and the refractive index of a 100 nm conformal HSQ cladding ($\Delta n_{cladding}$) were simulated with the Lumerical finite-difference mode eigensolver. Temperature dependence of the refractive index of GaP was estimated using the Sellemeier equation and corresponding coefficients for GaP as described in Ref. [6]. Relationships were assumed to be linear for the range of shifts considered.

Table 2.1. Simulation Results for Fundamental Wavelength

Physical Variable	Resonance Shift Rate	Parameter Range
Temperature (refractive index of ring)	0.07572 C^{-1}	20 C
Width	0.6516 nm^{-1}	-100 Å
Refractive index of 100 nm cladding	11.42	0.06

Table 2.2. Simulation Results for Second Harmonic Wavelength

Parameter	Resonance shift rate	Change in parameter
Temperature	0.05584 C^{-1}	20 C
Width	0.1129 nm^{-1}	-100 Å
Refractive index of 100 nm cladding	2.674	0.06

By looking at the resonant shifts for only a single mechanism, we can quickly see how double and triple resonance at a specific target wavelength is a completely intractable problem. Given two initial resonant wavelengths near 775 nm and 1550 nm respectively, the temperature point at which the fundamental (1550 nm) and twice the second harmonic (775 nm) intersect reflects

double resonance. With one tuning mechanism, we have no control over what absolute wavelength the two intersect at, and for some combinations of initial resonant wavelengths, the intersection may occur at a point beyond what is practically realizable. As an illustrative example, the resonant wavelength-temperature relationship for the fundamental and second harmonic resonances of an example device with initial resonant wavelengths $\lambda_{0,775} = 775.0\ nm$ and $\lambda_{0,1550} = 1550.5\ nm$ is plotted in Fig. 2.2.

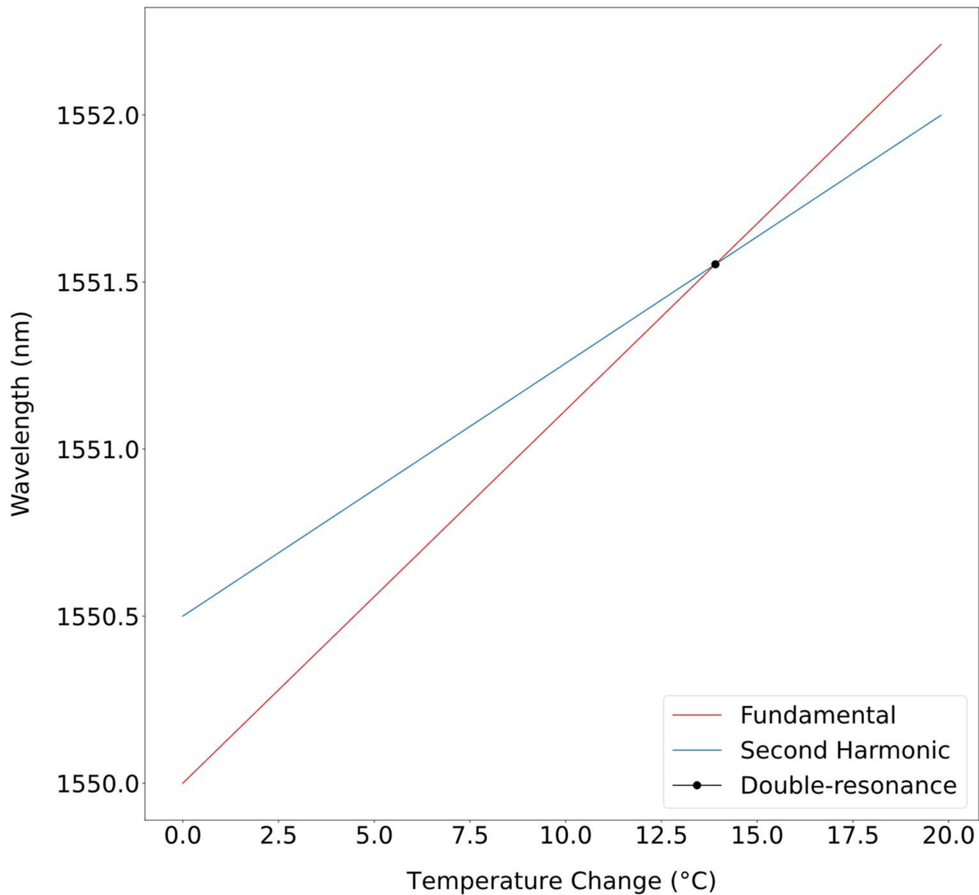

Figure 2.2. Plot of solution space for single-mechanism shifting

However, as we introduce additional tuning mechanisms the challenge becomes tractable. For the same second harmonic ring design as above, the inclusion of a second mechanism, here

$\Delta n_{cladding}$, expands the double resonance solution from a single point to a range of wavelengths over which double resonance may occur, denoted by the intersection of the two planes in Fig. 2.3.

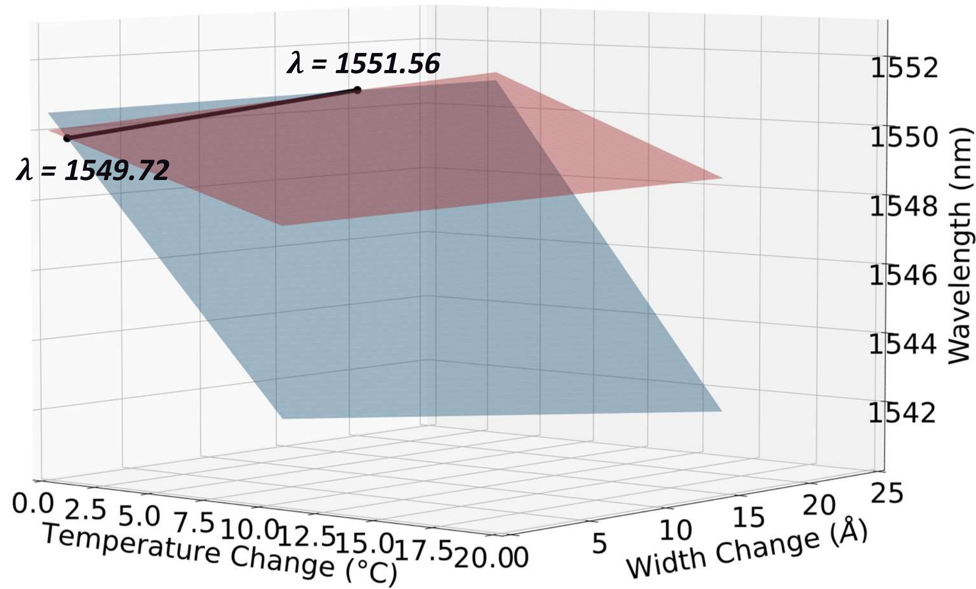

Figure 2.3. Plot of solution space for two-mechanism shifting.

With two mechanisms, the two-wavelength process of second harmonic generation at a specific target wavelength becomes possible. However, for triply resonant difference frequency generation devices, a third mechanism will be critical in achieving target-wavelength resonance of all three process wavelengths. To be able to tune any arbitrary set of two or three resonances to a specific target wavelength, we must develop an array of independent tuning mechanisms with varying rates of absolute and relative shift in resonance.

CHAPTER 3. BACKGROUND

3.1 RING RESONATOR DESIGN AND FABRICATION

3.1.1 *Digital Etching Experiment Devices*

The devices for digital etching experiments are fabricated from a 250 nm GaP membrane on an SiO_2 substrate. The devices are designed to be singly resonant at 1550 nm in the fundamental TE_{00} mode, with a radius of 4.7 μm and a waveguide width of 600 nm. The design was optimized with a residual 100 nm layer of HSQ resist on the top surface of the resonators from the fabrication process. 9 patterns of 18 devices were fabricated with a range of waveguide widths to account for fabrication tolerances. Each pattern included devices with coupling regions with designed coupling quality factors Q_c of 20k and 200k. The device layout includes two coupled waveguides, one with grating couplers at both the input and through ports, the other with a grating coupler at the drop port and a taper at the add port. This layout is shown in Fig 3.1.

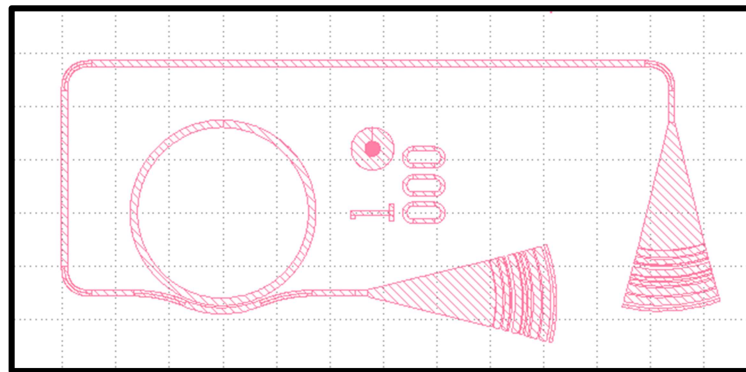

Figure 3.1. Digital etching device layout

The GaP membrane used to form the devices was grown by molecular beam epitaxy (MBE) on an $Al_{0.8}Ga_{0.2}P$ sacrificial layer on a GaP substrate. The GaP membrane was released from the substrate and transferred onto a thermal SiO_2-on-Si substrate using the membrane release process

of releasing the GaP from the sacrificial AlGaP layer in 3:100 HF:H2O, transferring the membrane to DI water, capturing the membrane on a water droplet on the oxide substrate, and drying at 80 C° [6]. The oxide substrate surface was cleaned and treated with hexamethyldisilizane vapor before transfer.

After transfer, the design described above was patterned onto the chip using e-beam lithography with a ~100 nm thick layer of HSQ e-beam resist, followed by a reactive ion etch (appendix A). This fabrication process can be applied to a diamond substrate for future GaP-on-diamond photonic circuits integrated with solid-state defects.

3.1.2 *HSQ Exposure Experiment Devices*

The devices for HSQ exposure experiments are fabricated from a 250 nm GaP membrane on an Si_3N_4 substrate. The rings are designed to be doubly resonant at the TE_{00} mode at 1550 nm and the TM_{03} mode at 775 nm to meet the quasi-phase matching condition for second harmonic generation. The devices have a radius of 7.77 μm and a waveguide width of 940 nm. The device layout consists of two grating-coupled input/output waveguides, one with a coupling region optimized for 1550 nm (coupling quality factors of 50k and 160k included), and the other for 775 nm (coupling quality factors of 18k and 56k). For design optimization, a 100 nm conformal cladding layer with refractive index n = 1.45 was included to reflect the tuning process. The device layout is shown in Fig 3.2.

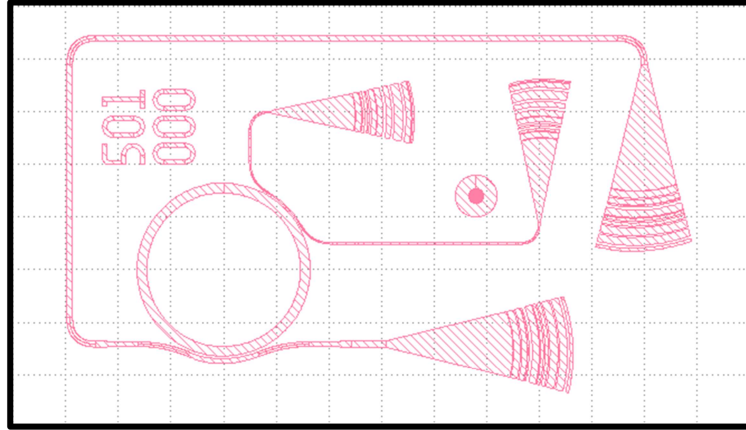

Figure 3.2. HSQ exposure device layout

For fabrication, a GaP membrane was released with the same process described in Section 3.1.1. However, before transfer, a 5 nm layer of SiO_2 was thermally evaporated onto the substrate, which was then treated with hexamethyldisilizane vapor. The chip was similarly patterned using e-beam lithography with a ~100 nm thick layer of HSQ e-beam resist followed by a reactive ion etch. In this fabrication process, a layer of developed HSQ e-beam resist remains on top of the GaP devices. To allow for a new, uniform coating of unexposed HSQ necessary for tuning, the residual layer must be removed. HSQ is removed by etching with HF, however HF also etches SiO_2; for this reason, Si_3N_4 was chosen as the substrate. Initial attempts at wet etching to remove the HSQ revealed low adhesion of the GaP membrane to the substrate: stiction from the wet process damaged the waveguide coupling regions. Instead, the residual HSQ layer was successfully removed with an HF vapor etch (Appendix A). The chip was then heated to 200 C^{o} to remove vapor-etch byproducts from the surface of the chip. Finally, a new ~100 nm layer of HSQ e-beam resist was spun on.

3.2 TESTING SETUPS

Testing for the following experiments consisted of transmission testing at the fundamental and second harmonic frequencies, as well as second harmonic generation collection using the confocal microscope configuration shown in Fig 3.5. For telecom transmission testing, the devices were excited over a 1530-1565 nm range using a Keysight 81682A tunable laser source amplified with a Thorlabs Erbium-Doped Fiber Amplifier (EDFA) 100P. Transmitter telecom signal was collected from the output telecom grating coupler by an IR photodiode. For near-infrared transmission testing, the devices were excited with a broad-spectrum Fianium WhiteLase Micro supercontinuum filtered to supply continuous output from 700 to 1200 nm . The transmission spectrum near 775 nm was collected from the near-IR waveguide grating coupler and detected by a grating spectrometer. Reflected input light for both setups was minimized by cross-polarizing the input and output signals and using a pinhole to spatially select the output grating.

For second harmonic generation testing, the fundamental mode was excited with the telecom tunable laser source and amplifier described above scanning over a 1530-1565 nm wavelength range. Second harmonic signal was collected from the near-IR grating coupler and measured on a Single-Photon Counting Module (SPCM). Telecom transmission was simultaneously measured at the telecom output grating coupler from signal transmitted through a Semrock MaxMirror to the telecom collection path.

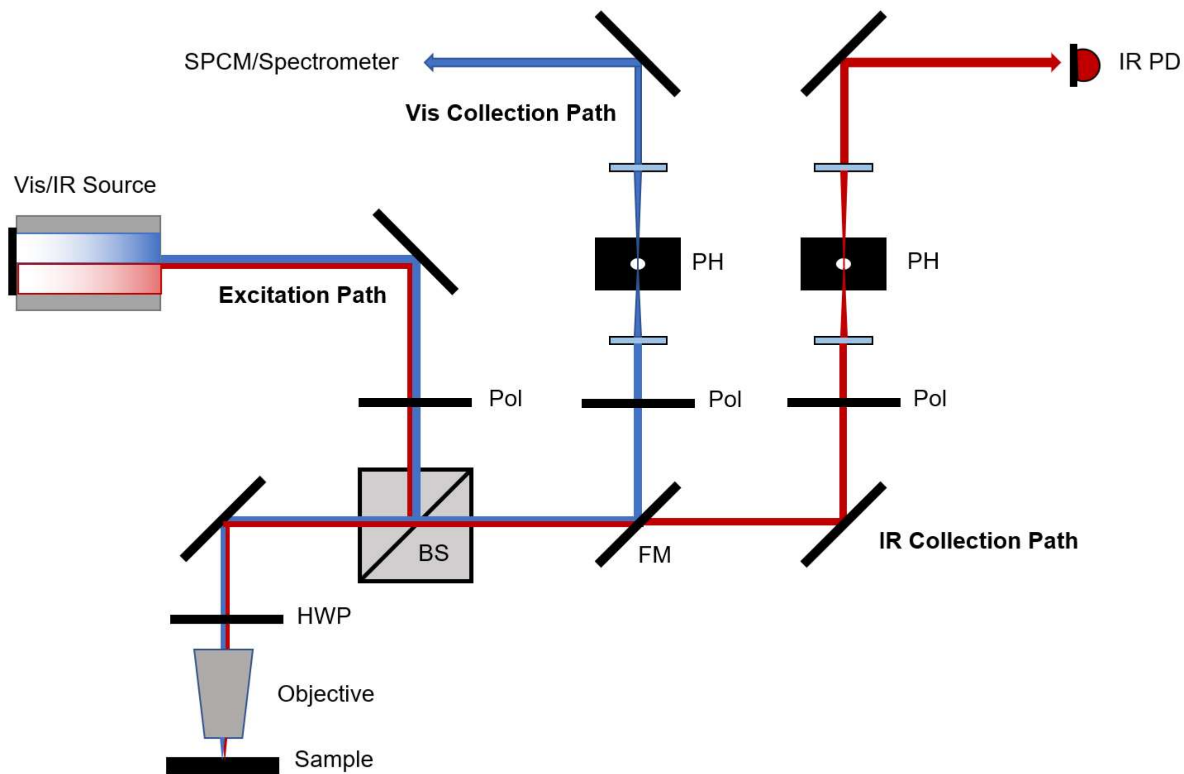

Figure 3.5: Confocal microscope for Vis/IR Transmission and SHG testing

Pol: Polarizer, HWP: Half wave plate, PH: Pinhole, PD: Photodiode, BS: Beamsplitter, SPCM: Single Photon Counter Module, FM: Flip mirror (Semrock MaxMirror).

CHAPTER 4. DIGITAL ETCHING

4.1 BACKGROUND

Traditional wet etching processes for III-V semiconductors like GaP work by combining an oxidizer and acid to continuously oxidize and then remove exposed layers of material. This process works too quickly to control with the angstrom-scale precision necessary for the required resolution in target-wavelength frequency tuning [14]. One way to better control this process is by digital etching, where oxidizer and acid are applied separately. In the first step, a diffusion-limited oxide layer is formed either by the atmosphere or an oxidizing solution such as hydrogen peroxide. Etching with acids such as hydrochloric acid removes only the newly formed layer while leaving the underlying resonator material untouched. Experiments applying this process to several different materials including gallium arsenide have succeeded in removing single 15 Å thick layers from gallium arsenide [14].This process has been used to tune gallium arsenide planar photonic crystal cavities in 2-3 nm steps [15]. Little research has been done on digital etching of gallium phosphide, however as III-V semiconductors with similar chemistries, gallium phosphide and gallium arsenide likely share similar digital etching properties.

4.2 SIMULATIONS

The predicted change in resonance from wet etching can be found using a finite difference eigenmode solver that calculates the spatial profile and frequency dependence of modes by

solving Maxwell's equations on a cross-sectional mesh of a device. The simulation can be used to find the effective index of refraction of the resonator at each step in the wet etching process. The simulated device has a width of 840 nm, a height of 437 nm, and a radius of 7.12 um. The top of the resonator is covered in 100 nm of HSQ resist. The resonator is simulated with its original width of 840 nm, a width of 837 nm with 1.5 nm of oxide on both sides, and a width of 837 nm.

From the three simulations, the effective index of refraction of the first radial TE mode at a wavelength of 1550 nm and the fourth radial TM mode at a wavelength of 775 nm which satisfy the second-harmonic quasi-phase-matching conditions can be found. The condition for constructive interference of a ring resonator can then be used to find the exact resonant wavelength at each step in the etching process.

At 775 nm, the indices correspond to a decrease in resonant wavelength of 0.81 nm when the oxide is grown and 0.97 nm (0.16 nm from post-oxidation) after the etching process is complete. At 1550 nm, the indices correspond to a decrease in resonant wavelength of 0.49 nm when the oxide is grown and 0.62 nm (0.13 nm from post-oxidation) after the etching process is complete. Thus, the resonances can be shifted by steps of less than a nanometer and can be shifted by approximately 0.3 nm relative to each other.

4.3 Experiment

The digital etching process was initially tested with an array of singly-resonant rings, using hydrogen peroxide as the oxidizer and HCl:H_2O(1:1) as the etchant. Telecom transmission tests were performed at each step of the process to determine the cavity resonances. First, the devices were etched with HCl:H_2O(1:1) for 1 minute to remove any native oxide and subsequently

telecom transmission tested. The devices were then submerged in hydrogen peroxide for 1 minute to form an oxide layer on the resonator sidewalls and telecom transmission tested. Finally, the devices were again etched with HCl:H_2O(1:1) for 1 minute to remove the resulting oxide layer and telecom transmission tested again.

Using only the growth of native oxide over several hours to form the stepwise etch layer was also tested by performing multiple sequential rounds of etching. Each etch was spaced out by approximately one hour with telecom transmission testing performed before and after every etch.

4.4 RESULTS

Resonances near 1550 nm were measured on 21 devices. After the oxidation step, a redshift of 0.300 ± 0.227 nm was observed. This shift is opposite in direction to the predicted value for oxidation. Following the etching step, an additional shift of -0.480 ± 0.261 nm was observed. This result more closely aligns with the predicted shift for the process. Most importantly, both steps show a significant range of error. Fig. 4.1 shows the cumulative wavelength shift for each device.

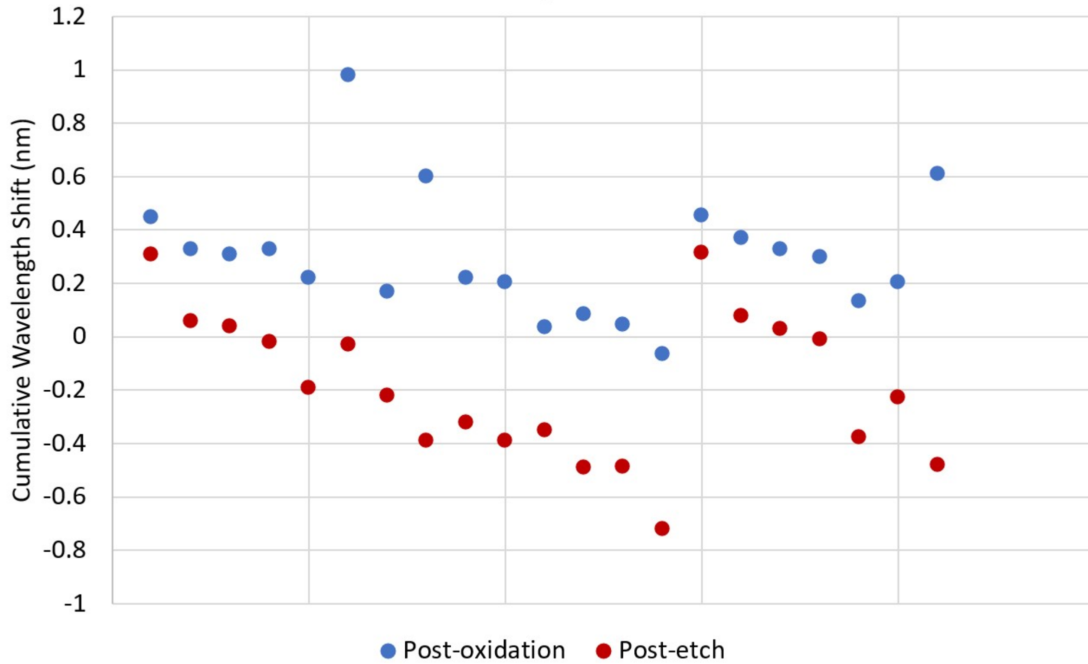

Figure 4.1. Plot of cumulative wavelength shift during digital etching process.

These results may potentially be explained by the fast formation of the native oxide following the etching process. In the period between the end of wet processing and transmission testing the devices are exposed to the atmosphere, allowing a new native oxide to form on exposed GaP. Thus, for the oxidation step the hydrogen peroxide is interacting with some thickness of oxide rather than GaP. For the etching step, some unknown thickness of oxide has formed before transmission testing post-etch. Observation of the resonance shift, presumably due to native oxide formation, is shown for a single device after one HCl:H_2O(1:1) etch beginning from five minutes (minimum possible time given experimental constraints) in Fig. 4.2.

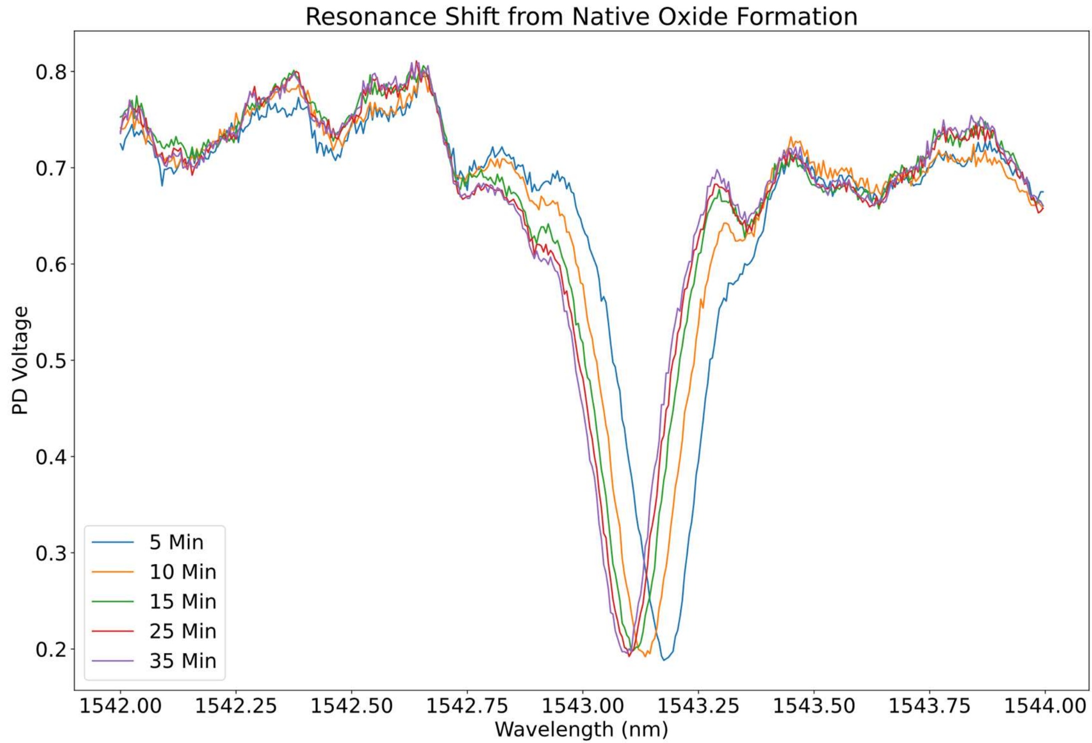

Figure 4.2. Plot of resonance shift of single device during native oxide formation.

The diffusion-limited growth of the oxide in atmosphere following each etching step is itself enough to act as the oxidizing step in digital etching, although the thickness of the oxide layer may be somewhat more uncertain. Sequential etching experiments showed that given a formation time of approximately one hour, a single etching step yields a shift of -0.379 ± 0.163 nm. Following eight rounds of etching, the sidewalls of a resonator were examined using a scanning electron microscope. Although changes in quality factor could not be quantitatively addressed due to thermal bistability from high input powers in initial transmission testing, the same fabrication process has previously been used to fabricate high-Q resonators. Imaging shows significant roughness of the sidewalls that suggests degradation from the initial state of the resonator.

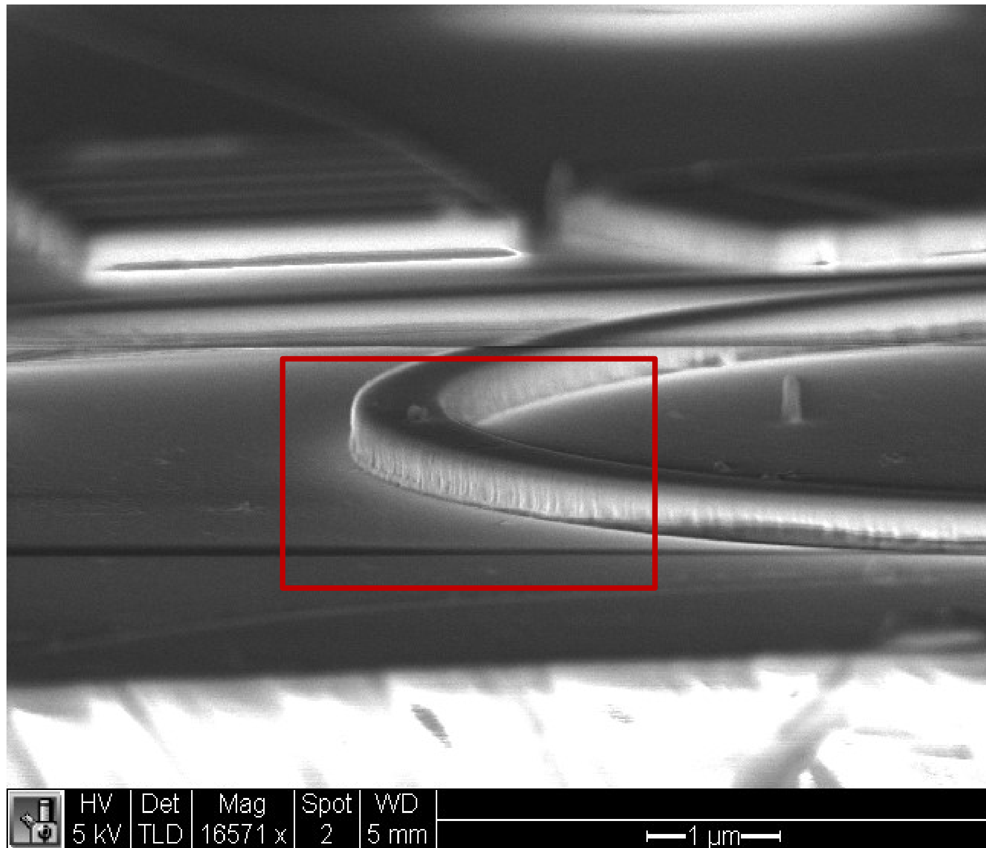

Figure 4.3.: Tilted SEM image of resonator sidewalls. Ring sidewall roughness clear in boxed region.

4.5 Conclusion

Testing of the digital etching process demonstrates that it can be successfully used in GaP devices to reduce resonator dimensions and blue-shift resonances in sub-nanometer steps. However, this method provides limited utility as a stand-alone method for post-fabrication trimming. For identical resonators in this experiment, resonances rarely vary by more than a few nanometers post-fabrication and are typically within a nanometer of each-other. The stepwise

nature of the process and the fast formation of a native oxide layer make tuning specific resonances to target wavelengths impractically difficult. Further experimentation of digital etching via native oxide formation, specifically on oxide formation-rate, may allow improved control over the process.

Another limitation of this process also lies in its potential degradation of the cavity sidewalls. For ring resonators little improvement in conversion efficiency of non-linear processes can come from optimizing mode-overlap in design. Rather, resonator quality factor is the limiting factor. Scattering losses due to surface roughness significantly impact quality factor. After eight etching cycles, the resonator sidewalls show roughness, possibly from residual fabrication process byproducts on the resonator sidewalls that cannot be etched by HCl. Identification of the specific cause of sidewall degradation may point towards etch processes that maintain device quality factor.

Despite its challenges, digital etching provides one key advantage in relation to other post-fabrication techniques; reduction of resonator dimensions remains the only way to blue-shift resonances. The issue of native oxide formation could be addressed by keeping the chip in an unoxygenated environment or depositing a cladding material. Any digital etching-based sidewall degradation for digital etching with these devices may be fabrication-process specific; attempts at digital and traditional etching with other materials have managed to maintain resonator quality factor with multi-nanometer dimension changes [11]. Identifying unknown byproducts resistant to etching may inform how to improve the digital etching process for GaP devices.

CHAPTER 5. HSQ EXPOSURE

5.1 BACKGROUND

Hydrogen silsesquioxane (HSQ) is a flowable oxide with a refractive index similar to SiO_2 (n~1.5) when cured. It is commonly utilized for surface planarization, encapsulation and as a high-resolution (sub 10 nm resolution) e-beam resist. HSQ is a promising candidate for post-fabrication trimming via cladding modification. Prior studies have focused on using thermal annealing to convert the cage-like structure of uncured HSQ into a denser networked silica structure [16], increasing the index of refraction of HSQ from n=1.45 to n=1.51 [17]. This change in chemical structure is shown in Fig. 5.1.

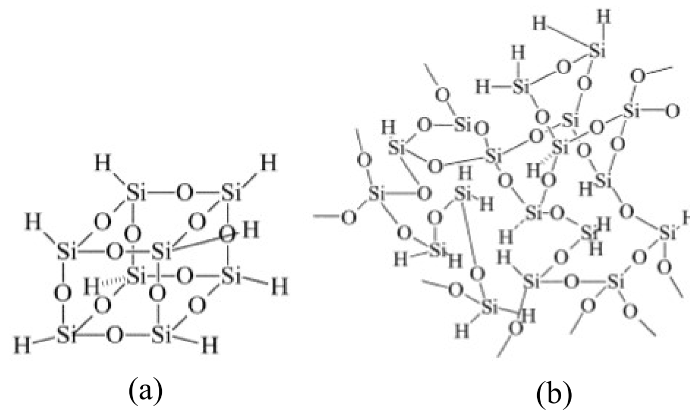

Figure 5.1. Diagram of (a) cage-form structure and (b) network-form structure of HSQ.

Localized laser annealing of HSQ on silicon microring resonators has been utilized to shift resonances by up to 1.1 nm without degrading resonance quality factors [17]. When HSQ is used as an electron-beam resist, e- exposure induces cross-linking, causing the same cage-to-network transformation. Using electron-beam exposure of HSQ presents a promising method for

trimming individual devices on a chip with high resolution and low loss that would be compatible with a wide range of materials, including GaP-on-diamond.

5.2 SIMULATIONS

The predicted shift from HSQ exposure was initially simulated with a finite-difference eigenmode solver. The simulated device dimensions reflect the devices fabricated for this experiment. The GaP ring resonator nominally has a height of 250 nm, waveguide width of 940 nm, and radius 7.77 μm. The ring is clad in a 100 nm-thick layer of HSQ. The variations in ring resonance wavelength for a change in effective index of refraction of the ring cladding from unexposed HSQ (n = 1.45) to fully exposed HSQ (n = 1.51) were calculated and are shown in Table 5.1.

Table 5.1: Simulated resonance shifts for HSQ exposure

λ	$\frac{d\lambda}{dn_{HSQ}}$	$\Delta\lambda$
1550 nm	46.133 nm	2.767 nm
775 nm	20.211 nm	1.213 nm

5.3 EXPERIMENT

The first goal of this experiment was to establish a relationship between exposure dosage and resonant wavelength shift that could be used to deterministically tune the resonant wavelength of individual devices on-chip. First, the residual HSQ from fabrication was removed. Then, a new ~100 nm conformal layer of HSQ resist was spun on (appendix A). Next, three identical sets of three devices were selected for a dosage test. For each device, transmission spectra in the fundamental and second harmonic bands were measured using the experimental setup described

in section 3.2 and analyzed to find resonance wavelengths and quality factors. Approximately 24 hours after HSQ spin-on, the devices from each set were exposed with electron beam doses of 1000, 1750, and 2500 μC/cm^2. The transmission measurements in both wavelength bands were repeated after exposure. The dosage test was repeated at 48 hours after spin-on with a group of devices identical to the first experiment to characterize any change in the dosage-shift relationship. Each day of the experiment and for several days following, both exposed and unexposed devices were repeatedly transmission tested at 1550 nm to monitor any global resonance shifts over time unrelated to exposure.

5.4 RESULTS

For the fundamental mode, the dosage test shows a clear linear relationship between resonant shift and exposure dosage, with maximum shifts up to ~3 nm, in good agreement with simulated shifts for $\Delta n_{HSQ} = 0.06$. The results of the dosage test for the fundamental wavelength are shown in Fig. 5.2. The change in n_{eff} at a certain wavelength depends strongly on the radial mode. For the same set of devices, the relationship between dosage and resonant wavelength shift is less evidently linear at the second harmonic wavelength (Fig. 5.3). At $\lambda = 775\ nm$, the quasi-phase matched mode for second harmonic generation is the TM_{03} mode. At $\lambda = 1550\ nm$, the quasi-phase matched mode is the TE_{00} mode. The TE_{00} mode is easily identified in IR transmission spectra, however at $\lambda = 775\ nm$, the device supports multiple modes that are difficult to distinguish, likely the source of uncertainty in a linear fit for the measured shifts.

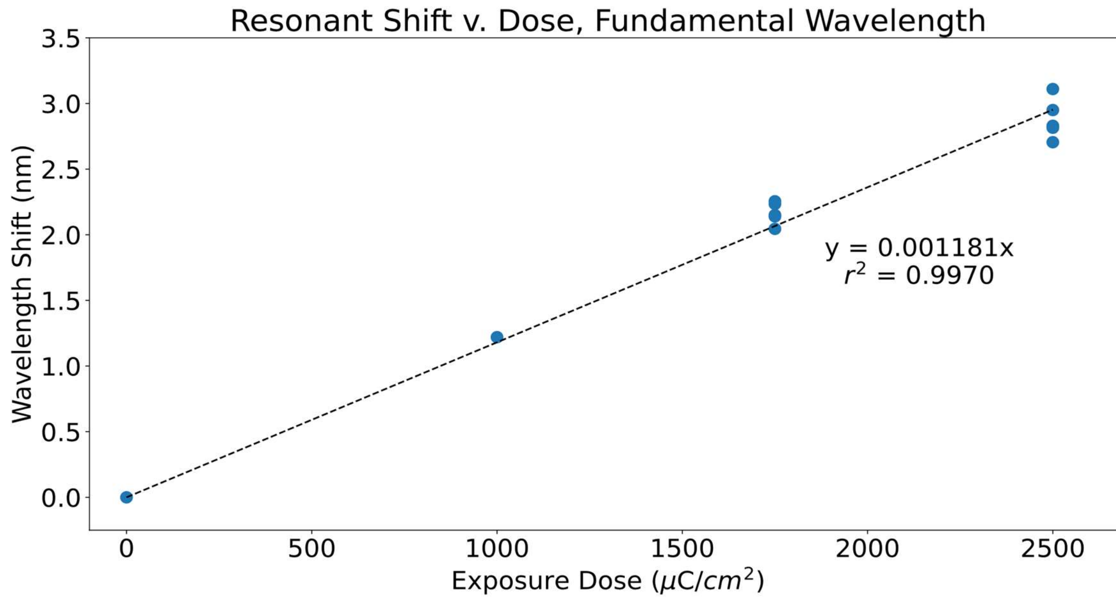

Figure 5.2. Plot of fundamental wavelength shifts for first dosage test.

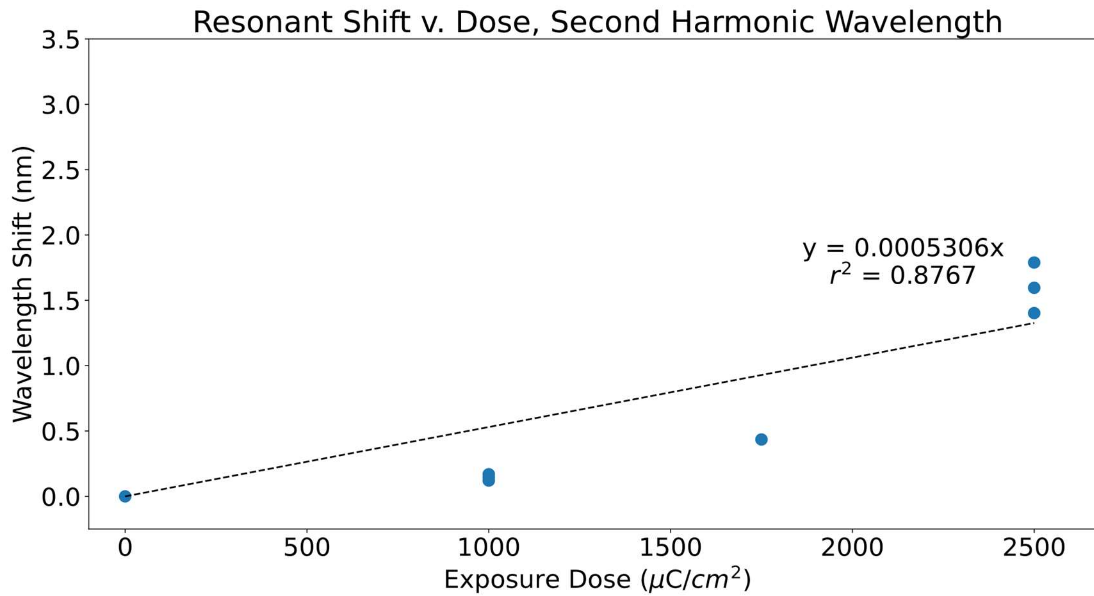

Figure 5.3. Plot of second harmonic wavelength shifts for first dosage test.

Further dosage tests demonstrate the relative stability of this relationship in the 48 hours following HSQ spin-on: $\frac{d\lambda}{dn_{HSQ}}$ changes by only -2.321E-5 nm, only 1.97% of the initial dependence (Fig. 5.4_. The y-intercept in the relationship shown in Fig. 5.4 reflects device drift over a 24-hour period between initial transmission testing and exposure.

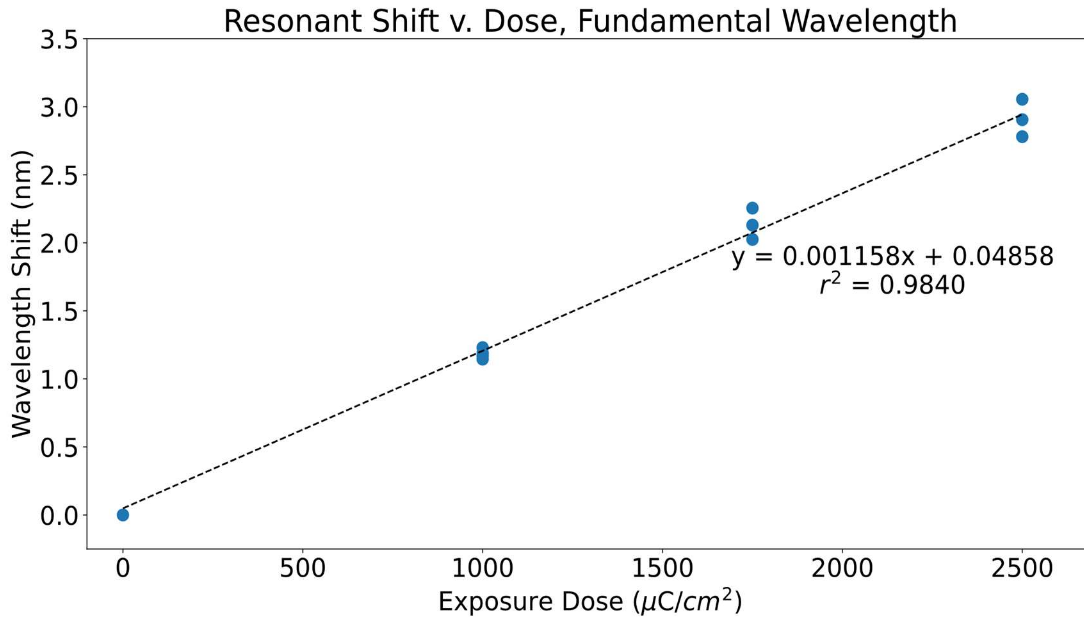

Figure 5.4. Plot of fundamental wavelength shifts for second dosage test.

One key concern about the practicality of any post-fabrication tuning mechanism is stability over time. For the devices from the first dosage test and three additional unexposed devices, the drift rate over the first five days following the experiment was 39.6 ± 18.7 pm/day. Fig. 5.5 shows the scale of the drift over five days compared to the shift from a 1750 μC/cm^2 exposure dose.

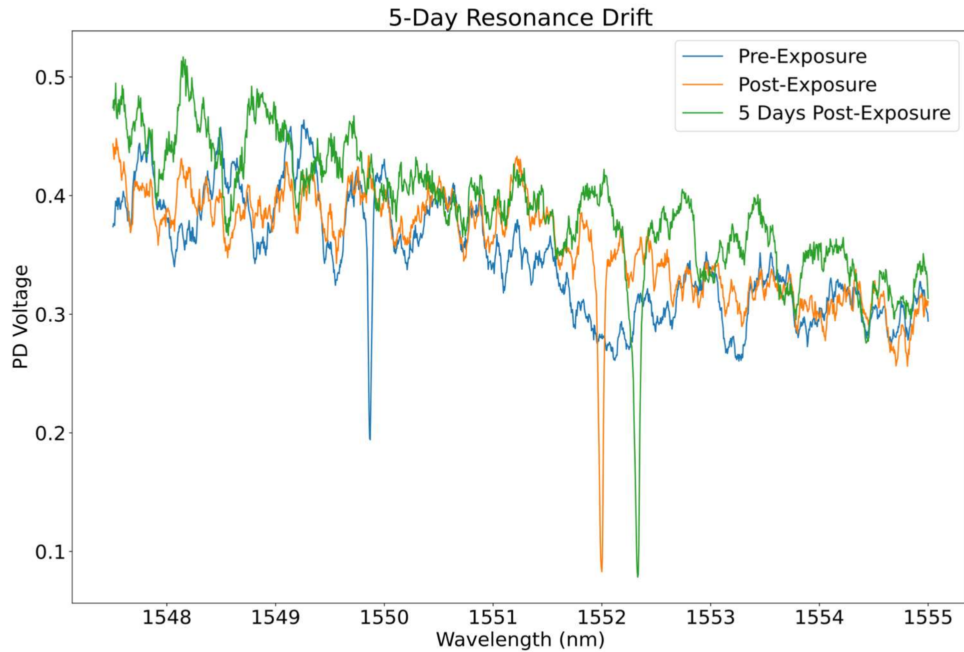

Figure 5.5. Plot of five-day resonance drift for fundamental wavelength

Another key concern for any tuning technique is resonator degradation. Methods that degrade the intrinsic quality factor of a device limit its ability to enhance input electric fields and reduce the efficiency of frequency conversion processes. Fig. 5.6 shows the distribution of change in normalized quality factor of 0.002 ± 0.386. The change in total quality factor for the devices is -1,800 ± 29,000.

Comparing pre- and post-exposure transmission shows some overall minor reduction in quality factor, however some devices show significant decrease or increase in quality factor. The distribution of changes in quality factor may be due to inconsistent changes in the waveguide coupling regions. The exposure pattern does not fully cover the waveguide coupling regions, thus changes in refractive index of the waveguide gap may not be consistent.

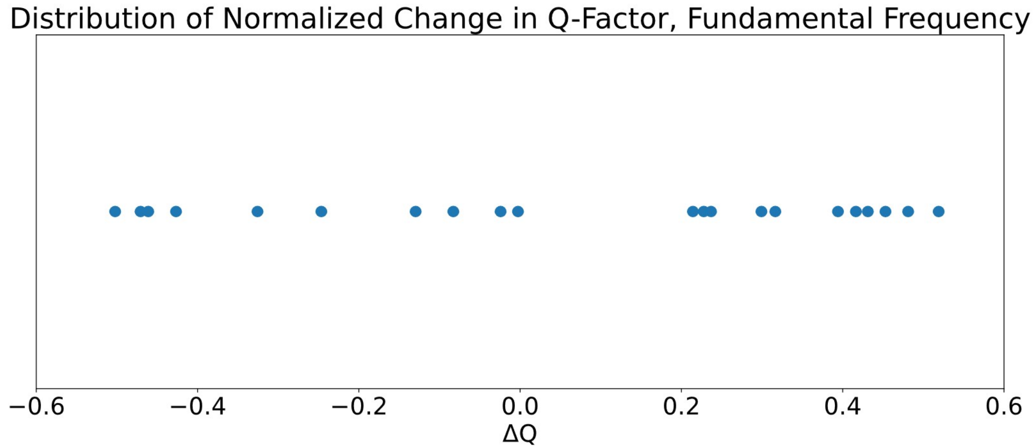

Figure 5.6. Distribution of normalized change in total quality factor at fundamental frequency

5.5 CONCLUSION

Shifts from HSQ exposure show a clear relationship with dosage at the fundamental wavelength that will enable deterministic tuning of individual devices to target input wavelengths. However, the unclear relationship for the second harmonic wavelength prevents characterization of the full solution space for a specific device. Without predictable shifts for both wavelengths, we cannot yet determine what combination of tuning mechanisms will enable quasi-phase-matched second harmonic generation at a target wavelength for any device. Consistent mode identification will be critical in future experiments that hope to incorporate rates for all wavelengths involved, especially for three-wavelength difference frequency generation.

Ideally any post-fabrication tuning technique should have no drift, allowing devices to indefinitely remain at the target wavelength. The next step in advancing HSQ tuning towards becoming a more robust tuning mechanism would be to determine whether the drift occurs due to interactions of the HSQ with the atmosphere. If such is the case, drift may be mitigated by the

incorporation of an additional cladding layer to separate the HSQ from the atmosphere and therefore stabilize it, which could even be incorporated pre-exposure.

Identifying the cause of distribution of change in quality factor is also key. Past experiments with HSQ annealing have not demonstrated any significant impact, indicating that loss introduced by this method is unlikely to be a significant issue [17]. However, characterizing how the coupling regions also behaves throughout this process will provide insight into ways to further optimize this process. Although HSQ generally requires high doses, at small doses shift magnitude was less predictable, potentially due to e-beam shot-noise at low exposure doses. If these hypotheses are confirmed, both changes in quality factor and low-dose shot noise could potentially be addressed by leveraging the control provided by e-beam exposure to experiment with variations in exposure pattern. Changes in quality factor could be made more consistent with better coupling region coverage in the write pattern. Low-dose shot noise could be mitigated by exposing only partial rings to higher doses.

In the long-term, e-beam exposure provides some other interesting avenues. Other works have shown that nano-meter-scale variations in ring inner radius can target specific modes for mode-splitting [18]. The resolution of e-beam exposure makes target mode trimming a realistic opportunity. This trimming method could also easily be applied to other photonic resonators such as inverse-design resonators [19]. Despite the need for further investigations in this process described here, the results demonstrated are enough to act as a useful tool in post-fabrication tuning for second harmonic generation devices.

CHAPTER 6. SHG WITH TARGET-WAVELENGTH TRIMMING

6.1 EXPERIMENT

The promising results of the HSQ exposure tests in Chapter 5 enabled an attempt at target-wavelength trimming of the fundamental mode with multiple devices on the same chip. First, a set of identical devices on the chip were IR-transmission tested to determine the initial post-fabrication resonant wavelengths. Given the resonant shift-dosage relationship found in Section 5.3, shift (nm) = 0.00118137 * dose (μC/cm^2), the solution space for each device is shown in Fig. 6.1. From the set of identical devices, devices 1, 2, and 3 were chosen to trim to a target wavelength of $\lambda = 1533.75\ nm$:.

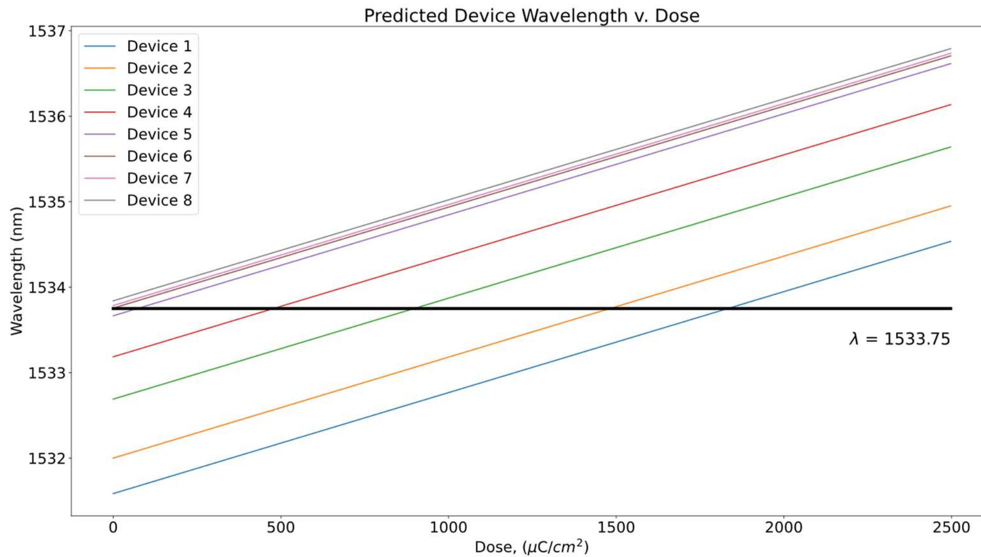

Figure 6.1. Predicted trimming behavior of identical SHG resonators.

Each device was exposed to a dosage calculated to tune the target resonance to $\lambda = 1533.75\ nm$, then lower dosages of 50-100 μC/cm^2 for fine trimming. At low doses, exposure produced less consistent resonance shifts with each incremental dose. After exposure, the

selected devices were again IR-transmission tested. The IR transmission spectra from before and after exposure illustrate the success of the process in trimming device resonances to a target wavelength. Fig. 6.2 shows the transmission spectra for the three devices before and after exposure. Using incremental steps, the three devices were all brought within 0.03 nm of the target resonance and each other. This range in trimming uncertainty is only slightly greater than one full-width-half-maximum (~0.025 nm) of the devices.

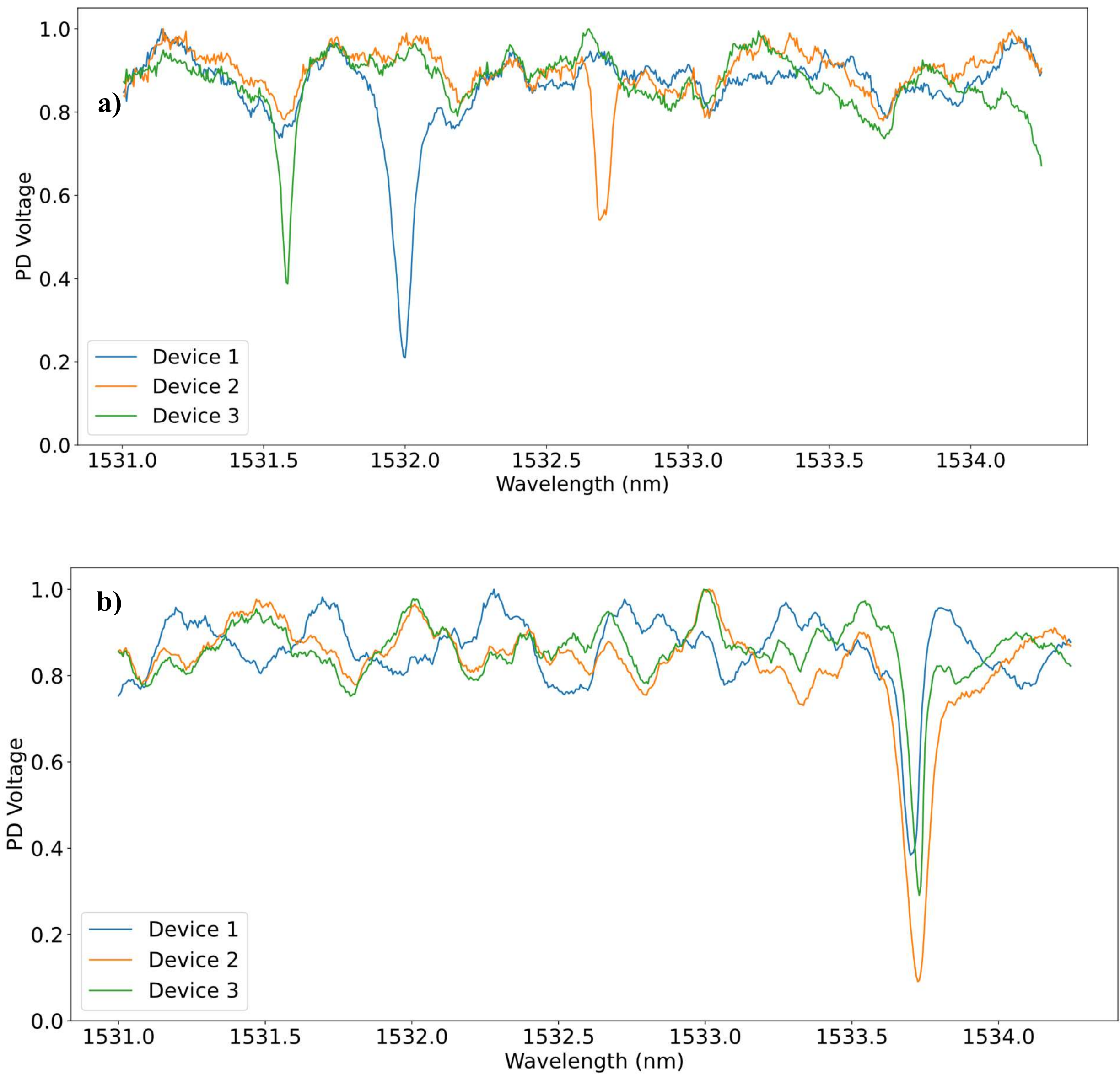

Figure 6.2. Transmission before (a) and after (b) 1533.75 nm target wavelength trimming

6.2 SECOND HARMONIC GENERATION IN TRIMMED RESONATORS

The three devices were SHG tested using the setup described in Section 3.2. Even without intentional trimming of the NIR resonances, all three devices display SHG at the target wavelength at room temperature.

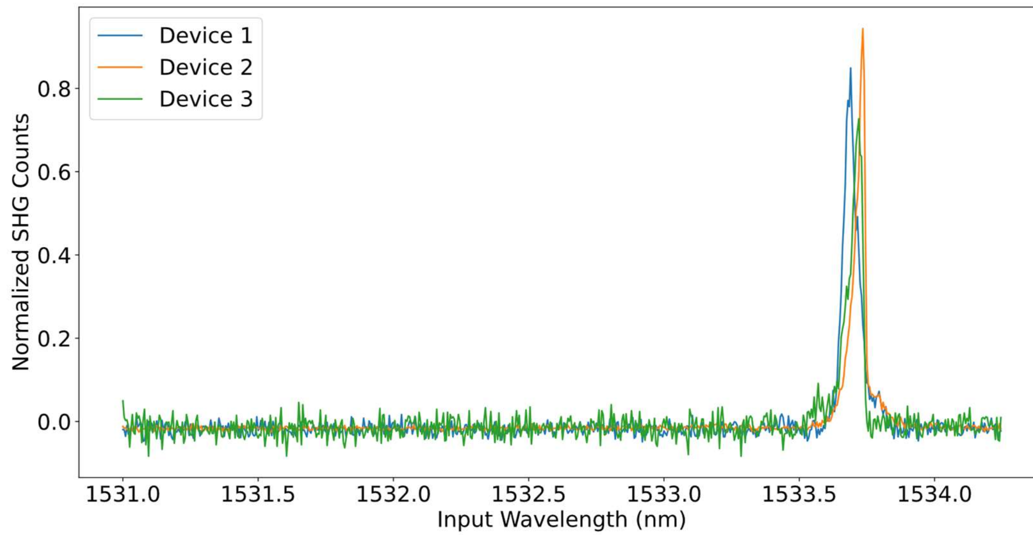

Figure 6.3. Target-wavelength SHG for three identical devices

Temperature tuning confirms near-quasi-phase-matching of the devices at room temperature. The intensity of SHG shows a strong temperature dependence as each device is tuned from 24.3°C to 29.3°C.

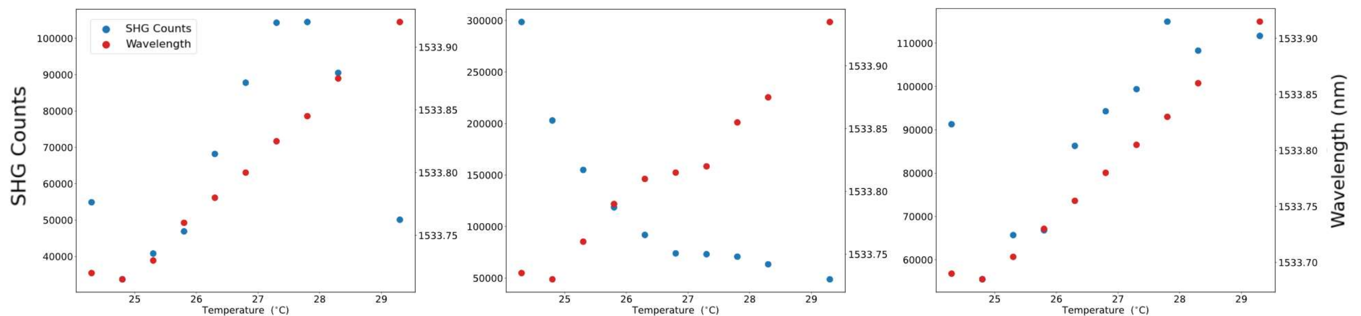

Figure 6.4. Temperature-tuning plots for devices 1, 2, 3

NIR transmission spectra of devices 1 and 2 (Fig. 6.5) demonstrate how the non-target-wavelength-trimmed NIR resonances create different temperature dependences for each device. While the fundamental modes are aligned, the second harmonic are not, causing peak SHG signal at different temperatures as the fundamental and second harmonic resonances come in and out of alignment with each other.

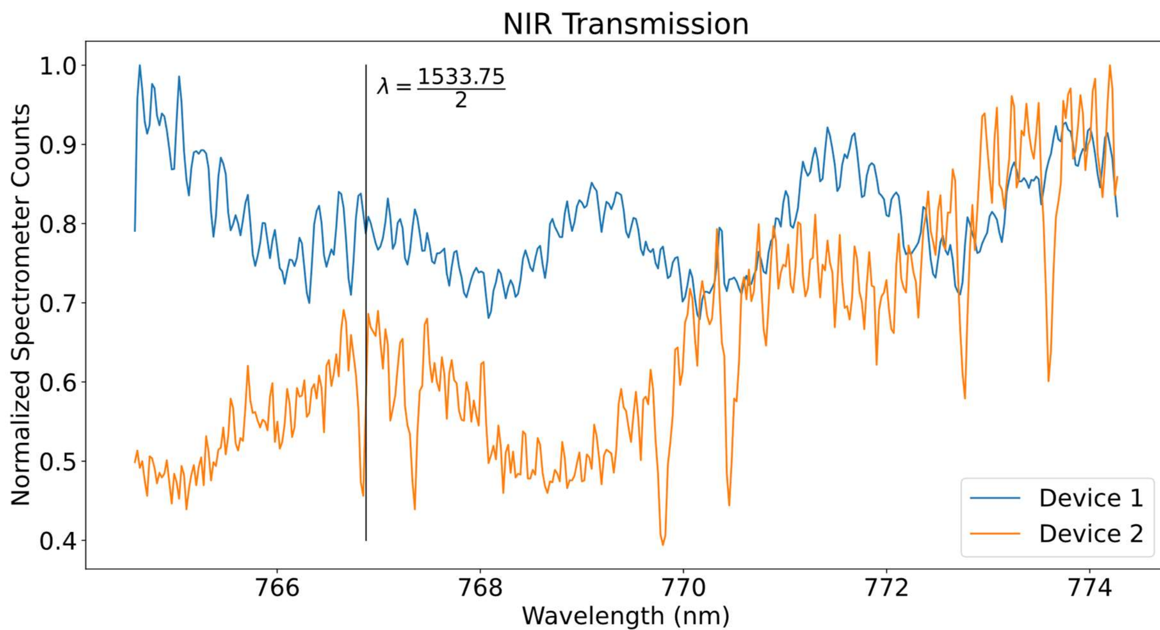

Figure 6.5. NIR transmission of device 1 and device 2 at room temperature

6.3 CONCLUSION

The shift-dose relationship established in Section 5.4 provides an easy method for target-wavelength trimming of the fundamental mode of devices designed for SHG. The addition of temperature tuning as a second tuning mechanism enabled all three devices trimmed to produce quasi-phase-matched SHG very near to the target wavelength. Despite a well-fit linear relationship stable over the time period of the experiment, delivering a single exact dose failed to

bring all devices to the target wavelength. With a more gradual process, significantly better control over resonant wavelength produced SHG at a target wavelength from all three devices. Multiple specific methods for improving this process may already be identified. Low dose shot noise presents a barrier to fine control over small wavelength shifts. This issue could be addressed by delivering higher doses to only part of a ring to produce a shift, although further investigation on whether this method also has a negligible impact on quality-factor is necessary. Looking further into the future of this technology, the process could be significantly improved by implementing simultaneous measurement and trimming capabilities, a feature that is only limited by the tools available rather than and quality of the process itself. Even through these preliminary SHG demonstrations, HSQ exposure has already confirmed its capabilities as a trimming mechanism.

CHAPTER 7. CONCLUSION AND OUTLOOK

This work has been motivated by the demand for post-fabrication tuning and trimming mechanisms that will help in bridging the gap between research and scalable technology for ring resonators for quantum frequency conversion. Through simulations I showed how a single tuning mechanism will not be enough; achieving both quasi-phase matched and target-wavelength SHG and DFG will require the development of multiple independent mechanisms. I identified resonator material, resonator dimensions, and cladding material as three independent variables that may be manipulated post-fabrication. Active resonance tuning via the thermo-optic effect has already been established as one useful mechanism. Based on previous works I identified one possible method each for resonator dimension and cladding material control. Digital etching has previously been used to etch away angstroms-thick layers of III-V materials similar to GaP with stepwise diffusion-limited oxidation and etching. I found that the process could be successfully harnessed for GaP resonators with some modifications and limitations. Oxidation with hydrogen peroxide yielded shifts in the direction opposite of those predicted and simulated. Digital etching via the similarly diffusion-limited formation of native oxide on exposed GaP produced consistent blue shifts under 0.5 nm, albeit with a large uncertainty relative to the size of shift. Observations of the fast formation of native oxide confirmed that digital etching under atmospheric conditions will both make consistent processing challenging and impact shift stability. Perhaps the most significant concern for the digital etching process is the potential introduction of additional sidewall roughness. For a technology whose efficiency relies strongly on resonator quality factor, the introduction of sidewall roughness would likely prevent this method from being useful. If these concerns may be addressed, atmospheric digital etching may act as a limited tool for coarse adjustment in post-fabrication tuning and trimming.

The second mechanism identified, HSQ exposure, shows potential as a highly useful method for fine adjustment of device resonances. The fundamental frequency shift-dose relationship identified supports the hypothesis that a highly consistent linear relationship exists for specific resonator modes. Further testing may confirm this for shorter resonant wavelengths. HSQ exposure excels against every metric set out in this work. The method is nearly lossless over a wide range of wavelengths It enables resonance control on the scale appropriate for frequency conversion devices. As a trimming method, it does not require active control. The method can be used to trim single devices on a chip. Resonance shifts remain fairly stable over time, although further research on the source of shifts may allow the mechanism to become even more stable. This mechanism may be further developed by improvements such as introducing simultaneous measurement and trimming capabilities. Even as an extremely immature process, HSQ exposure has demonstrated its promise by enabling simultaneous, target-wavelength-trimmed SHG from multiple identical devices on the same chip. Refinement of the HSQ exposure process will easily yield consistent, quasi-phase-matched, target-wavelength SHG from any device. Its success when applied to SHG devices suggests that HSQ exposure will be a profoundly useful post-fabrication trimming tool for DFG devices.

BIBLIOGRAPHY

[1] A. W. Elshaari, W. Pernice, K. Srinivasan, O. Benson and V. Zwiller, "Hybrid integrated quantum photonic circuits," *Nature Photonics,* vol. 14, p. 285–298, 2020.

[2] H. Bernien, B. Hensen, W. Pfaff, G. Koolstra, M. S. Blok, L. Robledo, M. Markham, D. J. Twitchen, L. Childress and R. Hanson, "Heralded entanglement bewteen solid-state qubits separated by three metres," *Nature,* vol. 497, pp. 86-90, 2013.

[3] B. Hensen, H. Bernien, A. E. Dreau, A. Reiserer, N. Kalb, M. S. Blok, J. Ruitenberg, R. F. L. Vermeulen, R. N. Schouten, C. Abellan, W. Amaya, V. Pruneri, M. W. Mitchell, M. Markham, D. J. Twitchen, D. Elkouss, S. Wehner, T. H. Taminiau and R. Hanson, "Loophole-free Bell inequality violation using electron spins separated by 1.3 kilometres," *Nature,* vol. 625, pp. 682-686, 2015.

[4] M. Pompili, S. Hermans, S. Baier, H. Beukers, P. C. Humphreys, R. N. Schouten, F. L. Vermeulen, M. J. Tiggelman, L. dos Santos Martins, B. Dirkse, S. Wehner and R. Hanson, "Realization of a multi-node quantum network of remote solid-state qubits," *Science,* vol. 372, no. 6539, pp. 259-264, 2021.

[5] E. F. Schubert, Light Emitting Diodes, Cambridge University Press, 2006.

[6] A. D. Logan, M. Gould, E. R. Schmidgall, K. Hestroffer, Z. Lin, W. Jin, A. Majumdar, F. Hatami, A. R. Rodriguez and K.-M. C. Fu, "400%/W second harmonic conversion efficiency in 14 µm-diameter gallium phosphide-on-oxide resonators," *Optics Express,* vol. 26, no. 33687, 2018.

[7] A. D. Corso, F. Mauri and A. Rubio, "Density-functional theory of the nonlinear optical susceptibility: Application to cubis semiconductors," *Physics Review B,* vol. 53, pp. 15638-15642, 1996.

[8] M. Gould, S. Chakravarthi, I. R. Christen, N. Thomas, S. Dagostar, Y. Song, M. L. Lee, F. Hatami and K. M. C. Fu, "Large-scale gap-on-diamond integrated photonics platform for nv center-based quantum information," *Journal of the Optical Society of America,* vol. B 33, pp. B35-B42, 2016.

[9] C. Bradac, W. Gau, J. Forneris, M. Trusheim and I. Aharonovich, "Quantum nanophotonics with group IV defects in diamond," *Nature Communications,* vol. 10, p. 5625, 2019.

[10] I. Shoji, T. Kondo, A. Kitamoto, M. Shirane and R. Ito, "Absolute scale of second-order nonlinear-optical coefficients," *Journal of the Optical Society of America B,* vol. 14, pp. 2268-2294, 1997.

[11] X. Lu, G. Moille, Q. Li, D. Westly, A. Singh, A. Rao, S. P. Yu, T. Biles, S. Papp and K. Srinivasan, "Efficient telecom-to-visible spectral translation through ultralow power nonlinear nanophotonics," *Nature Photonics,* vol. 13, pp. 593-601, 2019.

[12] R. Boyd, Nonlinear Optics, Academic, 2008.

[13] Y. Dumeige and P. Feron, "Whispering-gallery-mode analysis of phase-matched doubly resonant second-harmonic," *Physics Review A,* vol. 74, no. 063804, 2006.

[14] G. C. DeSalvo, C. Bozada, J. Ebel, D. C. Look and J. P. Barrette, "Wet Chemical Digital Etching of GaAs at Room Temperature," *Journal of the Electrochemical Society,* vol. 143, no. 11, pp. 3652-3656, 1996.

[15] K. Hennessy, A. Badolato, A. Tamboli, P. M. Petroff, E. Hua, M. Atature, J. Dreiser and A. Imamoglu, "Tuning photonic crystal nanocavity modes by wet chemical digital etching," *Applied Physics Letters,* vol. 87, no. 021108, 2005.

[16] C. M. Lampert, Solar Energy Materials, The Royal Society of Chemistry, 1979.

[17] V. Biryukova, G. J. Sharp, K. Charalambos and M. Sorel, "Trimming of silicon-on-insulator ring-resonators via localized laser annealing," *Optics Express,* vol. 28, no. 8, 2020.

[18] X. Lu, A. Rao, G. Moille, D. Westly and K. Srinivasan, "Universal frequency engineering tool for microcavity nonlinear optics: multiple selective mode splitting of whispering-gallery resonances," *Photonics Research,* vol. 8, no. 11, pp. 1676-1687, 2020.

[19] S. Molesky, Z. Lin, A. Piggott, W. Jin, J. Vuckovic and A. W. Rodriguez, "Inverse design in nanophotonics," *Nature Photonics,* vol. 12, pp. 659-670, 2018.

APPENDIX A: FABRICATION PROCESS DETAILS

Highly anisotropic Inductively Coupled Plasma (ICP) etching using chlorine-based etch chemistries.
Recipe Name: 'FuLab GaP etch loop 2'
RF= 41W at 240V DC bias
ICP = 60W
Gas = Ar:Cl2:N2 :: 6:1:1 sccms
Chamber pressure = 3mT
Chuck temperature = 18C
Duration = 4x 33s loop with 30s intermediate no-plasma cooldown step
Carrier = Si wafer
Expected etch depth is ~550 nm (The GaP layer is only 250nm, but we always overetch as local etch rate can vary as a function of topology)
The addition of N2 enables formation of a passivating layer (possibly GaN) on the sidewalls resulting in higly anisotropic vertical sidewall profile.

SPTS uEtch vHF:

This HF Vapor Dry Etch system is configured with Hydrofluoric and Ethanol vapor used, primarily, for isotropic etching of silicon dioxide without a plasma. The HFVapor system etches at reduced pressure and 45C to isotropically etch sacrificial silicon oxide layers, primarily to release silicon microstructures in MEMS devices. The dry process avoids stiction of released moving parts and damage to delicate structures – common issues with conventional wet processing technology. This is a single wafer system for 4 inch to 8 inch wafers and dies on a carrier wafer.
Before running vHF sample is barrel etched @100W for 1.5min to remove any polymer residue (from gel pack)
Recipe etch rates are measured on a full 100mm SiO2 wafer. Etch rate for tiny samples are much higher (scales with exposed SiO2 area; i.e. loading effect)!
recipe 1 (did not note down the gas flow rates - will update);
Measured etch rate = 5.4nm/min; duration = 300s;
Expected thermal oxide etch depth = 300/60 * 5.4 = 27nm
The vHF process can produce residue that is volatile at elevated temperatures. Hence, the samples are heated to 200C for 5mins after vHF.
HSQ spin-on:

[Typically we deposit a 5nm SiO2 adhesion layer via e-beam evaporation prior to HSQ spin-on; however we don't do it for HSQ trimming]
HSQ is 6% solution in MIBK
First dehydrate the samples at 150C for 4min
1s ramp to 500 rpm, hold 1s
1s ramp to 6000 rpm hold 45s
3s ramp to 0 rpm
Soft-bake at 80C for 4min to remove Solvent
This gives ~120 to 150nm thick resist